

# Piezoelectrically-induced ultrasonic lubrication by way of Poisson effect

Sheng Dong, Marcelo J. Dapino

Smart Vehicle Concepts Center, Department of Mechanical and Aerospace Engineering,  
The Ohio State University, Columbus, OH 43210, USA

## ABSTRACT

It has been shown that the coefficient of dynamic friction between two surfaces decreases when ultrasonic vibrations are superimposed on the macroscopic sliding velocity. Instead of longitudinal vibrations, this paper focuses on the lateral contractions and expansions of an object in and around the half wavelength node region. This lateral motion is due to the Poisson effect (ratio of lateral strain to longitudinal strain) present in all materials. We numerically and experimentally investigate the Poisson-effect ultrasonic lubrication. A motor effect region is identified in which the effective friction force becomes negative as the vibratory waves drive the motion of the interface. Outside of the motor region, friction lubrication is observed with between 30% and 60% friction force reduction. A “stick-slip” contact model associated with horn kinematics is presented for simulation and analysis purposes. The model accurately matches the experiments for normal loads under 120 N.

**Keywords:** Piezoelectric actuator, Poisson effect, ultrasonic lubrication, contacting model

## 1. INTRODUCTION

Friction is the resistance to the relative motion between two objects sliding in contact with each other. Ultrasonic lubrication refers to the friction reduction that occurs when ultrasonic vibrations, that is vibrations at frequencies above 20 kHz, are applied in a direction collinear with the macroscopic sliding velocity. Being solid state, this phenomenon has significant fundamental and technological interest in applications in which lubricants are undesirable, such as certain aerospace components or human-machine interfaces. Further, the ability to modulate the friction force between a low and a high state can be advantageous in applications like adaptive vehicle suspensions, steering mechanisms, and powertrain components.

Ultrasonic lubrication was first studied by Mason<sup>1</sup> for reducing wear in electrical relays, and studies on the effect were published by Pohlman and Lehfeldt in the 1960's.<sup>2</sup> More recently, it has been researched by Littmann et al.<sup>3</sup> both experimentally and analytically through Coulomb friction modeling. Littmann et al.<sup>4</sup> developed the curve shown in Fig. 1, in which the friction ratio  $\mu_i$  is the ratio of friction force with ultrasonic vibrations over the native friction force, and the velocity ratio  $\zeta$  is the sliding velocity over the ultrasonic vibration velocity. It was shown that the relationship between  $\mu_i$  and  $\zeta$  is

$$\mu_i = \begin{cases} 1 & \zeta \geq 1, \\ (2/\pi) \sin^{-1} \zeta & -1 \leq \zeta \leq 1, \\ -1 & \zeta \leq -1. \end{cases} \quad (1)$$

A low friction ratio  $\mu_i$  corresponds to effective friction reduction. If the sliding velocity is high, so is  $\zeta$  and according to Fig. 1, the friction ratio is large resulting in low or null friction reduction. Thus, for a given sliding velocity, the velocity of the ultrasonic vibrations has to be sufficiently high for  $\mu_i$  to be as low as possible. This can be achieved by increasing the frequency or amplitude of the ultrasonic waves. The degree of friction reduction can be controlled by modulating the working ultrasonic power. Because friction is a system property,

---

Further author information: (Send correspondence to M.J.D.)

M.J.D.: E-mail: dapino.1@osu.edu, Telephone: 1 614 688 3689

S.D.: E-mail: dong.121@osu.edu, Telephone: 1 614 736 1818

Industrial and Commercial Applications of Smart Structures Technologies 2012, edited by Kevin Farinholt, Steven F. Griffin,  
Proc. of SPIE Vol. 8343, 83430L · © 2012 SPIE · CCC code: 0277-786X/12/\$18 · doi: 10.1117/12.916404

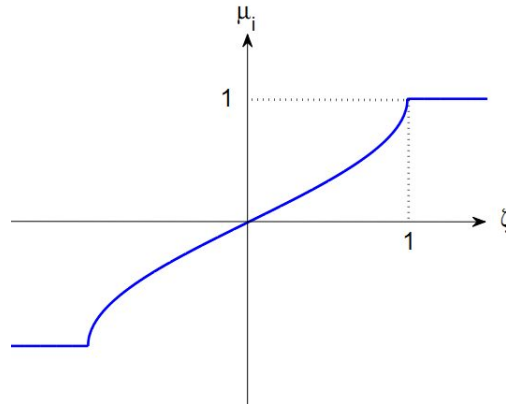


Figure 1. Friction ratio versus velocity ratio for ultrasonically lubricated system.<sup>4</sup>

the effectiveness of ultrasonic lubrication is affected by several system properties. Bharadwaj and Dapino<sup>5,6</sup> studied the dependence of friction reduction on ultrasonic sliding velocity, normal load, contact stiffness, and system stiffness.

In none of these studies has the lateral expansion of a solid driven by the Poisson effect under ultrasonic vibrations been the means for achieving friction reduction. In all prior art, the ultrasonic vibrations were applied in the same plane as the sliding interface either parallel or transverse to the sliding motion, whereas in this paper, it is desired that the ultrasonic vibration created by the Poisson effect be perpendicular to the sliding plane. Due to the Poisson effect, the longitudinal vibration of the horn induces vibration through the thickness of the vibrating object. The combination of vibrations in two orthogonal directions leads to elliptical movement of points located at the interface between the sliding objects, creating a different type of friction reduction mechanism. This mechanism is potentially more effective than the conventional in-plane modes of vibration.

This paper shows how Poisson-effect ultrasonic vibrations affect the dynamic friction coefficient between surfaces under various conditions including different material combinations and normal loads. A cube-type model is presented which describes the Poisson-effect friction reduction for low to moderate normal loads.

## 2. FINITE ELEMENT ANALYSIS

A finite element simulation was implemented in COMSOL Multiphysics 4.2 to calculate the Poisson-effect vibration of the horn subjected to force excitation on one side face. The first axial modes for the aluminum and stainless steel horns are 20.6 kHz and 20.8 kHz, respectively. Since the drive frequency for the welder is 20 kHz, the first axial modes dominate the vibration of both horns. The axial strain from horizontal vibration of the horn causes lateral strain, which makes the vibration at the bottom surface of the horn follow an elliptical pattern.

The locus curves of the vibration are shown in Fig. 2 for three different locations: Point 0 (centerline of the bottom surface of the horn), Point -1 (1 in to the left of the centerline), and Point +1 (1 in to the right of the centerline). The motion at locations -1 and +1 follows an overall elliptical trend. Such motion generates contact forces which push points on the horn surface towards the centerline. We refer to this phenomenon as *motor effect*, and we consider it similar to the motor force encountered in piezoelectric ultrasonic motors. Theoretically, the entire flat surface of the bottom of the horn should be subjected to symmetric motor forces pushing points towards the centerline. However, it is observed experimentally that around the centerline the motor force is negligible due to the small vibration amplitude associated with the half-wavelength node. We refer to this region with negligible motor effect as *transition region*. In this region the motion of points on the surface of the horn is random. The approximate dimensions of the motor effect regions and transition regions measured experimentally for aluminum and stainless steel are shown in Table 1.

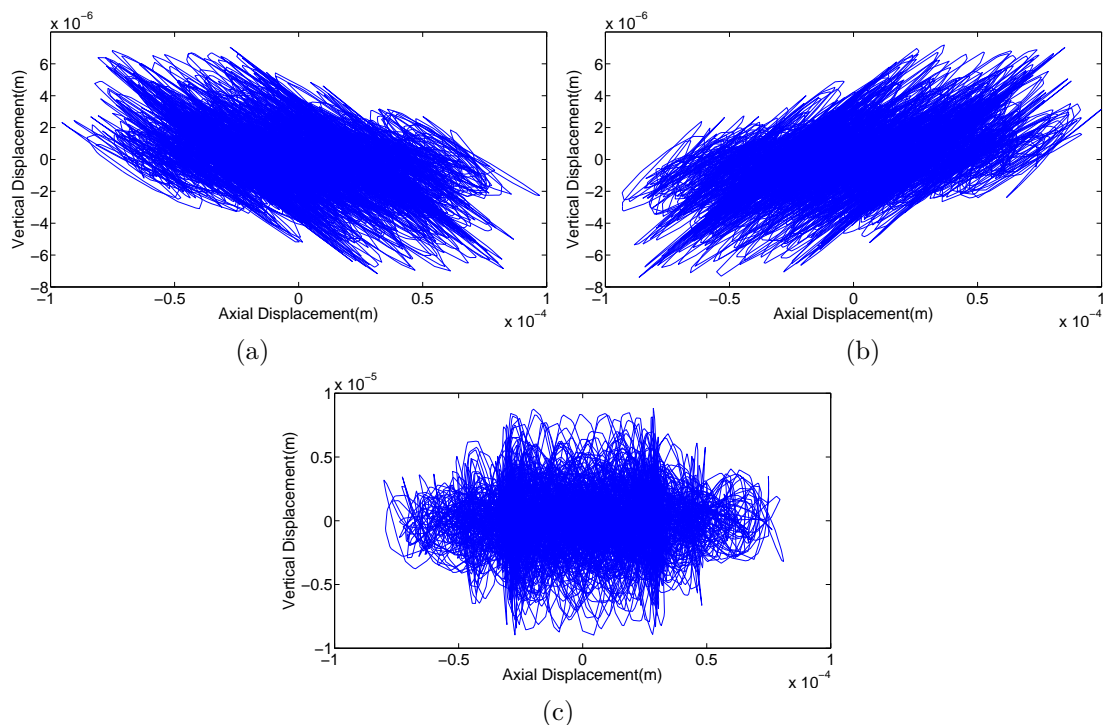


Figure 2. Locus curves of the vibrations at points on the horn surface [(a) point -1; (b) point +1; (c) point 0].

Table 1. Approximate dimensions of the transition and motor effect regions for the aluminum and stainless steel horns.

Horn	Transition region	Motor effect (left)	Motor effect (right)
Aluminium	-0.25 in to +0.25 in	-1.5 in to -0.25 in	+0.25 in to +1.5 in
Stainless steel	+0.1 in to +0.2 in	-1.5 in to +0.1 in	+0.2 in to +1.5 in

### 3. EXPERIMENTS

#### 3.1 Experimental setup

An experiment was developed using a commercial ultrasonic welder (Dukane 220) as the source of vibrations. When connected to its dedicated power supply, this welder reliably supplies 20 kHz sinusoidal signals at various discrete power levels (25, 50, 75, and 100% of the full 8.5 micron amplitude, 2.2 kW power machine limit). As shown in Fig. 3, vibrations from the welder are transmitted to a horn with dimensions 5 in (127 mm) by 2.4 in (60.96 mm) by 1 in (25.4 mm). A block with a curved top surface slides underneath the horn, creating a line contact with the bottom surface of the horn. Two different materials were chosen for the horn and sliding block, stainless steel and aluminum. Tests were conducted for three material combinations (aluminium horn on stainless steel block, stainless steel horn on aluminium block, and stainless steel horn on stainless steel block).

In order to investigate the Poisson-effect ultrasonic lubrication, which is expected to be most effective around the half-wavelength node region, the system was tested with the interface between the horn and sliding block within  $\pm 1$  in ( $\pm 25.4$  mm) of the centerline of the horn. In this manner, both the transition and motor effect regions are characterized. The block is given a sliding velocity of 0.2 in/s (5 mm/s) under normal loads from 60 N to 240 N supplied by a screw connected to a load frame. Low-friction pads located between the “top piece” and the horn minimize the tangential force created by friction between these two components. Load cells measure the normal force exerted by the screw and tangential force required to displace the sliding block.

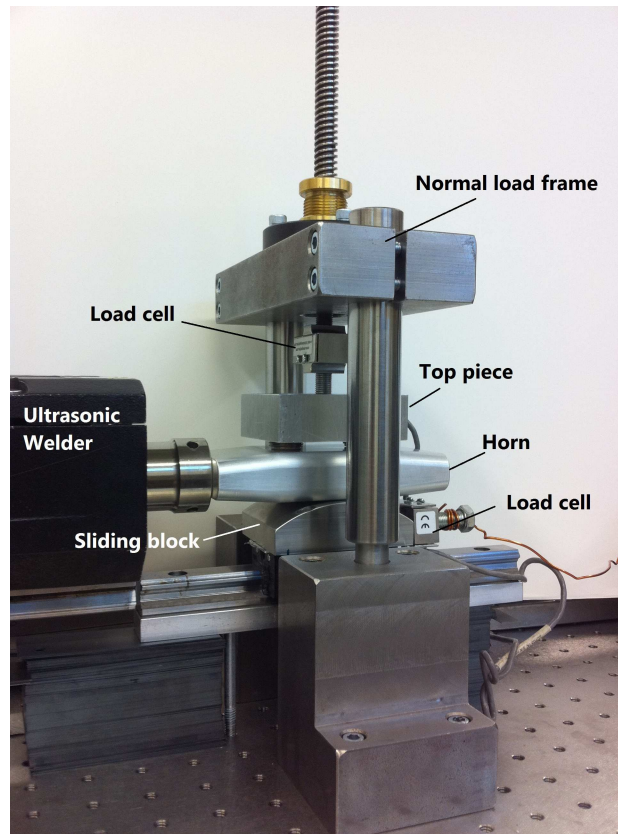


Figure 3. Experiment developed to investigate the Poisson-effect ultrasonic lubrication.

### 3.2 Friction reduction in motor effect regions

The first group of tests was conducted at location -1 with no externally applied tangential force acting on the sliding block. The sliding block was observed to experience a net contact force from the piezoelectric vibrations which creates macroscopic motion toward the centerline of the horn. The motor force thus overcomes the static friction coefficient, giving an effective friction reduction of more than 100%. Similar results were obtained from the tests conducted at location +1. The motor force was quantified from the reading of the tangential load cell with the sliding block fixed at either the -1 or +1 position (Fig. 4). This measurement was conducted for the aluminum horn and stainless steel block. As shown in Fig. 5, the net motor force increases linearly as the normal force increases.

### 3.3 Friction reduction in transition region

Tests conducted in the transition region for the aluminum horn and stainless steel sliding block are shown in Fig. 6(a). The data shows a relatively linear relationship between tangential and normal forces both without and with ultrasonic power applied. In order to calculate the effective friction coefficients, points were extracted from the data as shown in panel (b). The dynamic friction coefficients are reduced from approximately 0.55 without ultrasonic vibration to approximately 0.35 with ultrasonic power applied. The percent friction reduction, shown in panel (d), hovers around 40% for all normal forces.

The measurements and calculated friction reduction curves for the other two material combinations are presented in Fig. 7 and 8. For the combination of stainless steel horn and aluminium block, the dynamic friction is reduced by 25 to 48%. For the combination of stainless steel horn and stainless steel block, the friction is reduced by 50 to 56%. The stiffer material combination gives greater friction reduction, as expected in general.

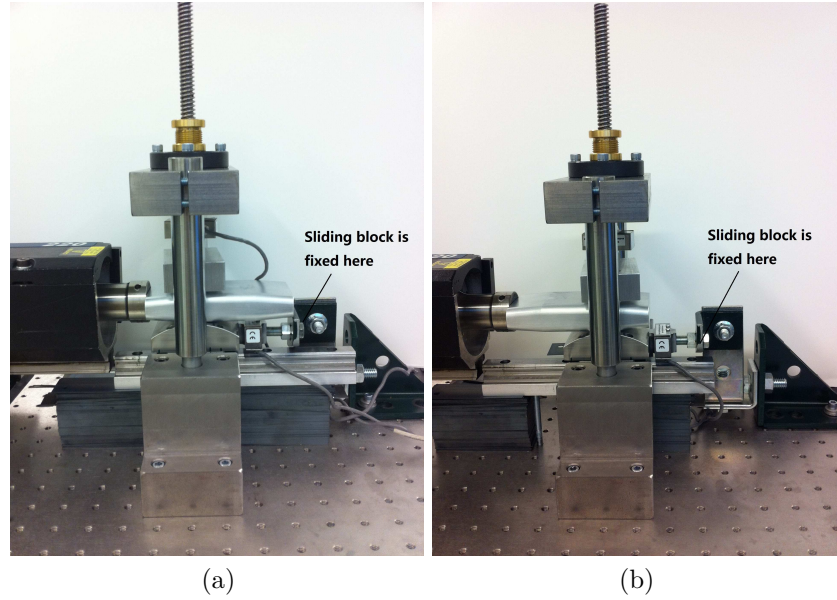


Figure 4. Test set-up for quantifying the net motor force: (a) point -1 and (b) point +1.

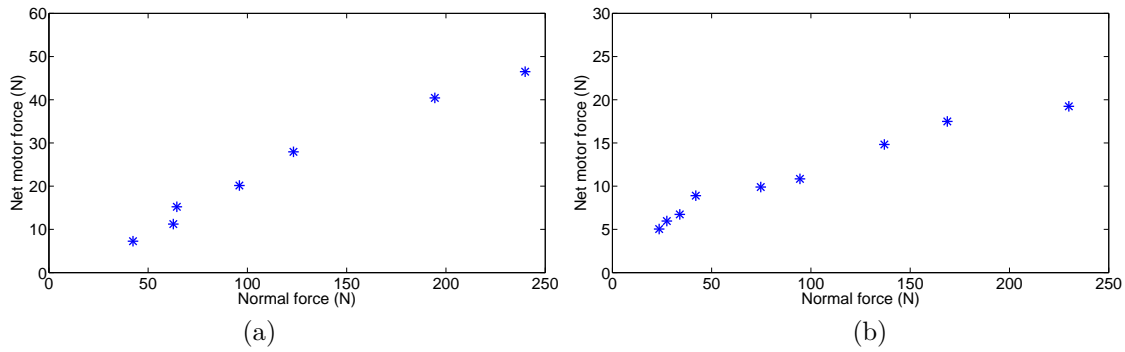


Figure 5. Relationship between normal force and net motor force: (a) point -1 and (b) point +1.

## 4. ANALYTICAL MODEL

### 4.1 Horn kinematics

Calculation of horn kinematics illustrates how the horn vibrates under the ultrasonic actuation. To simplify the analysis, the tapering and rounded edges of the horn were not taken into consideration. A simplified model of the horn is shown in Fig. 9. For a free-free end horn with length  $L$ , the motion can be described by superimposition of the motions of all modes,

$$u(x, t) = \sum_{n=1}^{\infty} (A_n \sin \omega_n t + B_n \cos \omega_n t) U_n(x), \quad (2)$$

where  $\omega_n$  is the  $n$ -th order frequency and  $U_n(x)$  is the function of  $n$ -th order mode shape. Let  $\beta = \omega/c_0$ , where  $c_0$  is the axial speed of propagation. It has been shown that<sup>7</sup>

$$\frac{\partial^2 U}{\partial t^2} + \beta^2 U = 0, \quad (3)$$

where  $U = C \sin \beta x + D \cos \beta x$ . Substitution of the the boundary conditions  $\partial u(0, t)/\partial t = 0$  and  $\partial u(L/2, t)/\partial t = 0$ , it is derived that  $C = 0$  and  $\sin \beta L = 0$ , thus  $\beta L = n\pi$  ( $n = 0, 1, 2, \dots$ ). Therefore, the order frequencies are  $\omega_n = n\pi c_0/L$  ( $n = 0, 1, 2, \dots$ ). When  $n = 1$ , the frequency is called half-wavelength frequency,  $f = \omega_n/(2\pi) = c_0/(2L)$ ,

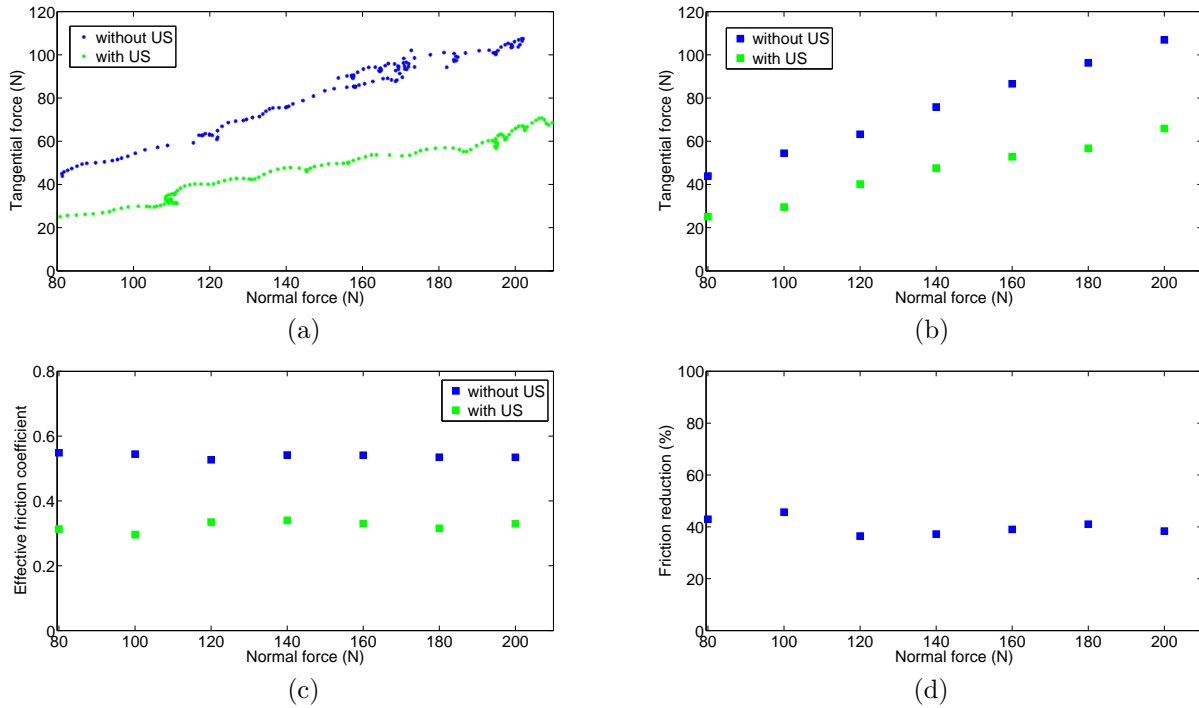


Figure 6. Transition region data for the aluminium horn and stainless steel block. (a) Measured normal forces and tangential forces. (b) Points extracted from the data at 20 N intervals. (c) Relationship between normal forces and friction coefficients calculated from the points in panel (b). (d) Friction reduction percentage as a function of normal load.

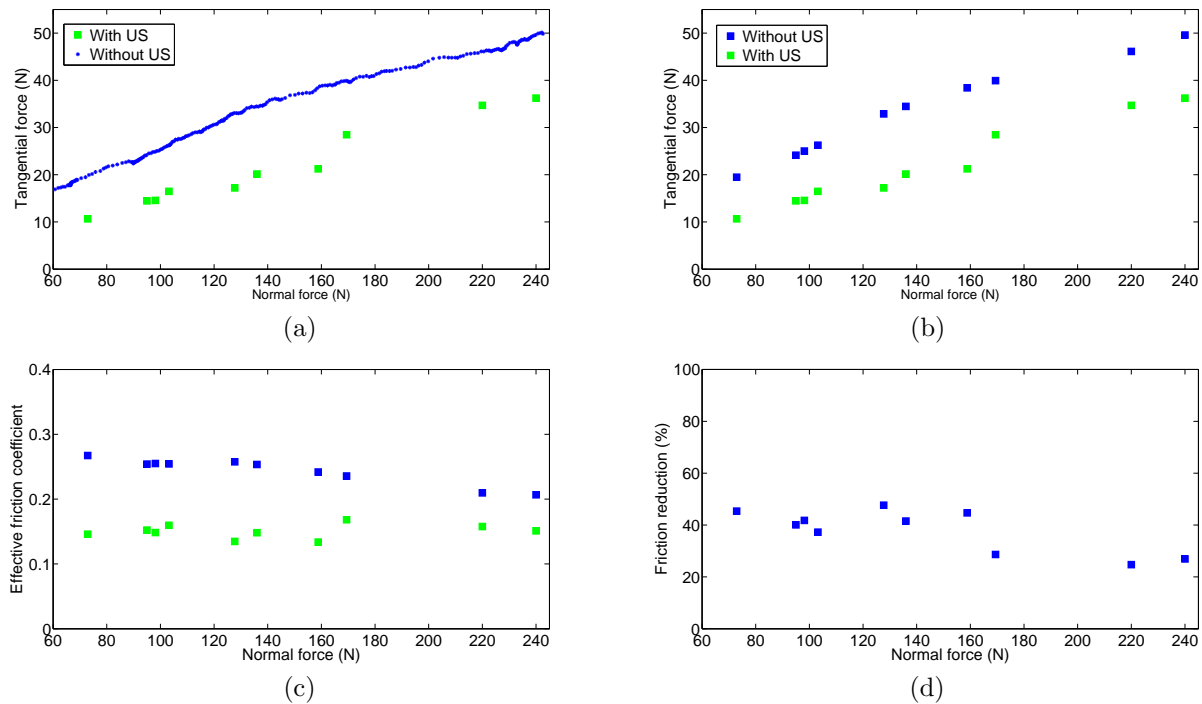


Figure 7. Data, reduced data, calculated friction coefficients, and calculated friction reduction for the stainless steel horn and aluminum block.

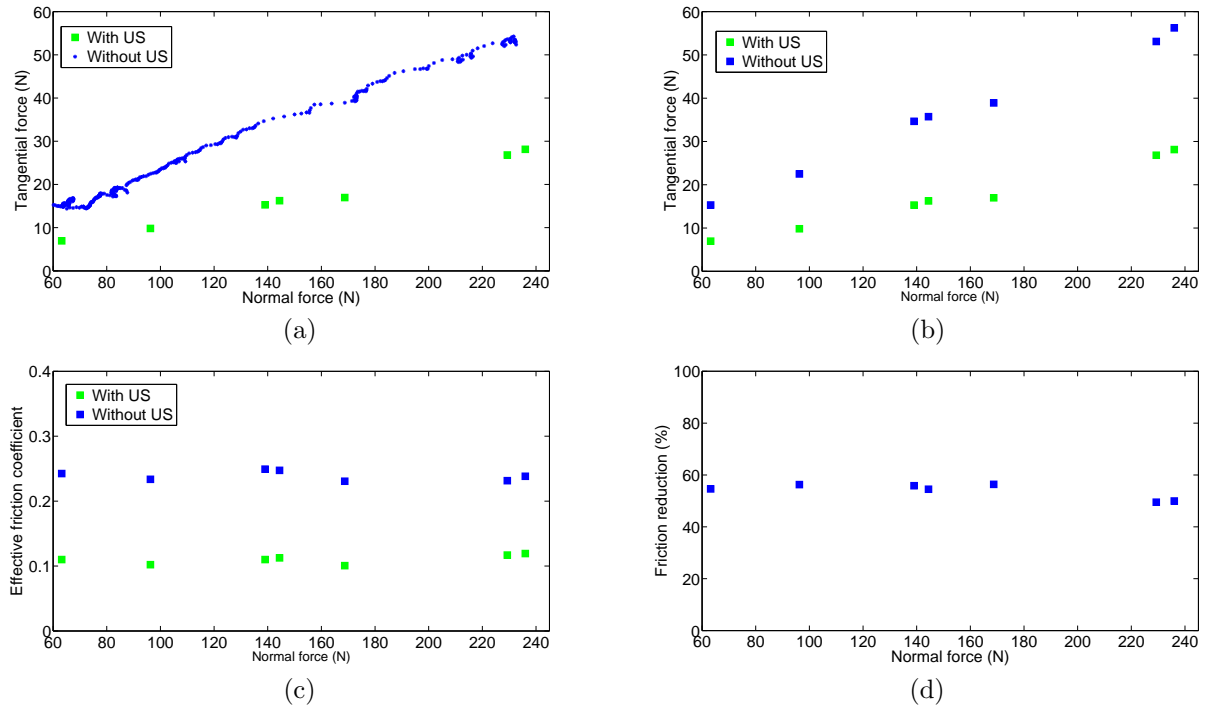


Figure 8. Data, reduced data, calculated friction coefficients, and calculated friction reduction for the stainless steel horn and stainless steel block.

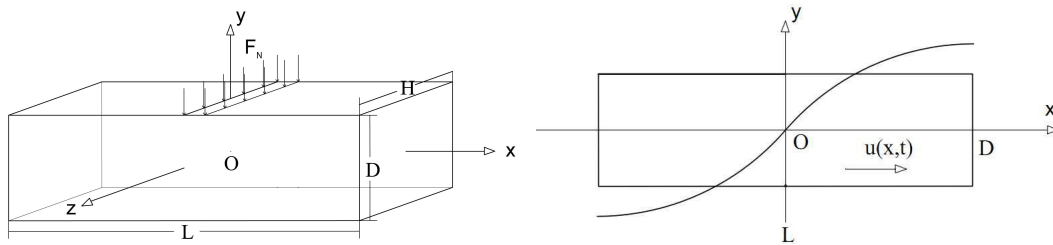


Figure 9. Illustration of the horn kinematics.

and the mode shape is as shown in Fig. 9. For stainless steel and aluminium, the bar velocities are respectively  $1.99 \times 10^5$  in/s ( $5.06 \times 10^3$  m/s) and  $2.06 \times 10^5$  in/s ( $5.23 \times 10^3$  m/s), thus the have-wavelength frequencies of the horns are 19.9 kHz and 20.6 kHz, respectively. Since the actuation frequency is 20 kHz, the first axial mode is dominant. The first axial mode follows a sinusoidal function, thus the axial displacement function is written as

$$u_x(x, t) = A \sin(2\pi ft) \sin\left(\frac{\pi x}{L}\right). \quad (4)$$

The axial strain of the horn is written as

$$\varepsilon = \frac{\partial u(x, t)}{\partial x} = \frac{A\pi}{L} \sin(2\pi ft) \cos\left(\frac{\pi x}{L}\right). \quad (5)$$

For isotropic materials, Hooke's law has the form<sup>8</sup>

$$\begin{cases} \varepsilon_x = \frac{1}{E} \{ \sigma_x - \nu(\sigma_y + \sigma_z) \} \\ \varepsilon_y = \frac{1}{E} \{ \sigma_y - \nu(\sigma_x + \sigma_z) \} \\ \varepsilon_z = \frac{1}{E} \{ \sigma_z - \nu(\sigma_x + \sigma_y) \}. \end{cases} \quad (6)$$

In this case,  $\sigma_x$  and  $\sigma_y$  arise from the axial vibration and the normal loads but  $\sigma_z$  is null. Thus, the horn strains can be written as

$$\begin{cases} \varepsilon_x = \frac{1}{E} \{ \sigma_x - \nu\sigma_y \} \\ \varepsilon_y = \frac{1}{E} \{ \sigma_y - \nu\sigma_x \}, \end{cases} \quad (7)$$

whereas the stresses in the  $x$  and  $y$  direction are calculated as

$$\begin{cases} \sigma_x(x, t) = E\varepsilon_x(x, t) = \frac{AE\pi}{L} \sin(2\pi ft) \cos\left(\frac{\pi x}{L}\right) \\ \sigma_y(x, t) = \frac{F_N}{A_0}. \end{cases} \quad (8)$$

where  $A_0$  is the contact area of the interface between the top piece and the top surface of the horn. Substitution of (8) into (7) gives

$$\begin{cases} \varepsilon_x = \frac{A\pi}{L} \sin(2\pi ft) \cos\left(\frac{\pi x}{L}\right) - \frac{F_N\nu}{EA_0} \\ \varepsilon_y = \frac{F_N}{EA_0} - \frac{A\pi\nu}{L} \sin(2\pi ft) \cos\left(\frac{\pi x}{L}\right). \end{cases} \quad (9)$$

Thus, the displacements can be integrated from strains as

$$\begin{cases} u_x = A \sin(2\pi ft) \sin\left(\frac{\pi x}{L}\right) - \frac{F_N\nu}{HE} \\ u_y = \frac{F_N D}{2EA_0} - \frac{DA\pi\nu}{2L} \sin(2\pi ft) \cos\left(\frac{\pi x}{L}\right), \end{cases} \quad (10)$$

where  $D$  is the thickness of the horn.

## 4.2 Contact model

Asperities are present in all surfaces.<sup>9</sup> As shown in Fig. 10, the contact between two nominal flat surface is in fact between asperities. Therefore, the actual contact area is much smaller than the nominal contact surface. A cube is used to represent the combined asperities. It is assumed that  $A_{r0}$  is the area of the top surface of the cube which is equal to the actual contact area. The shear stresses  $\tau$  are distributed evenly over the top surface and  $d_0$  is the average height of all contacting asperities. Therefore, when the ultrasonic vibrations are off, the native friction force is calculated as

$$F_{T0} = \tau_0 A_{r0} = \frac{G\Delta l_0 A_{r0}}{d_0}, \quad (11)$$

where  $G$  is the shear modulus of the cube and  $\Delta l_0$  is the shear deformation of the cube under friction force. As discussed in previous sections, when the ultrasonic power is turned on, the points on the surface of the horn follow an approximately elliptical locus. When the horn surface moves down to press the block surface, the friction force increases to a larger value than the natural dynamic friction so that there is no relative movement



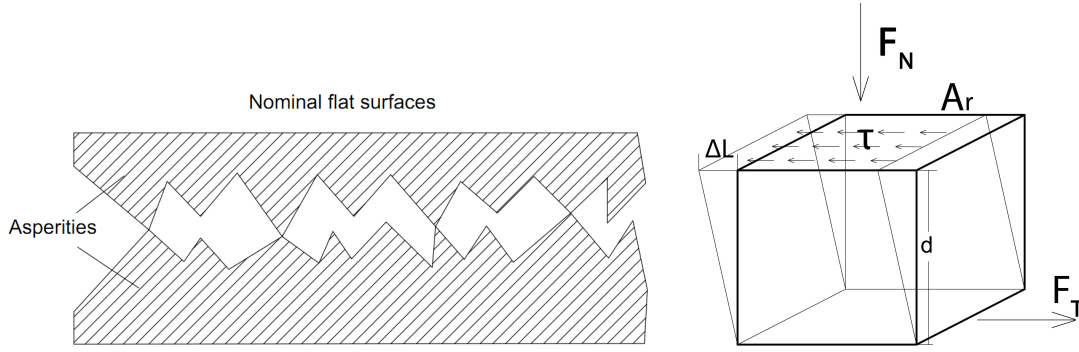


Figure 10. Asperities at the interface between two surfaces and “cube” model.

between the two surfaces. This is called the “stick” stage. When the horn surface moves up away from the block surface, the friction force decreases which enables relative motion under a lower friction. This is called the “slip” stage. The sliding between the horn and the block consists of a series of “stick” and “slip” events that take place alternately. The overall friction is the friction of the “slip” stage.

The motion of the horn changes the contact parameters and the dimension of the cube. The new shear deformation is  $\Delta l = \Delta l_0 + u_x$  and the new height of the cube is  $d = d_0 + u_y$ . Since the motion of the horn creates different contact stress at the interface, the real contact area also changes due to deformation of the asperities. Assuming that the asperity deformation is overall elastic, the friction force with ultrasonic power on is calculated as

$$F_T = \tau A_r = \frac{G \Delta l_0 A_r}{d_0} = \frac{G (\Delta l_0 + u_x) A_r}{d_0 + u_y}. \quad (12)$$

The normal loads are known from measurements, and the average height of the asperities can be calculated using,<sup>10</sup>

$$d = -\frac{R_q}{\lambda} \ln \left[ \frac{F_N(d) \lambda^{\frac{5}{2}}}{c \sqrt{\pi} R_q R_s E^* A_n} \right] \left( \frac{R_s}{R_q} \right)^{\frac{1}{2}} \quad (13)$$

where  $A_n$  is the nominal contact area,  $\eta$  is the areal asperity density of contact surface,  $R_q$  is the deviation of asperity heights of contact surface,  $R_s$  is the asperity radius of the contact surface,  $E^*$  is the combined Young’s modulus of two contacting materials calculated as  $1/E^* = 1/E_1 + 1/E_2$ .  $c = 17$ , and  $\lambda = 3$  are constants obtained from experiments. The actual contact area is calculated as

$$A_r = \frac{F_N(d)}{E^*} \left( \frac{\pi \lambda R_s}{\sigma} \right)^{\frac{1}{2}}. \quad (14)$$

### 4.3 Simulation results

Simulation results for the aluminum horn and stainless steel block are shown in Fig. 11. The model and test results match well for normal loads lower than 120 N. A comparison of the friction reduction between test results and model simulations is shown in Fig. 12. There is a discrepancy when the normal load is greater than 120 N. The discrepancy could be caused by plastic deformation or modulus change under high normal stress. A new model for a broader range of normal loads is being developed to address the mismatch.

## 5. CONCLUDING REMARKS

This paper presents an experimental and analytical study of ultrasonic lubrication created by Poisson-effect excitation. The ultrasonic horn was designed to exhibit two distinct regions. In the motor effect regions, the friction forces are fully cancelled by the motor force generated by the ultrasonic vibrations. The friction reduction in this region is 100%. In the transition region, the friction reduction percentages vary with different material

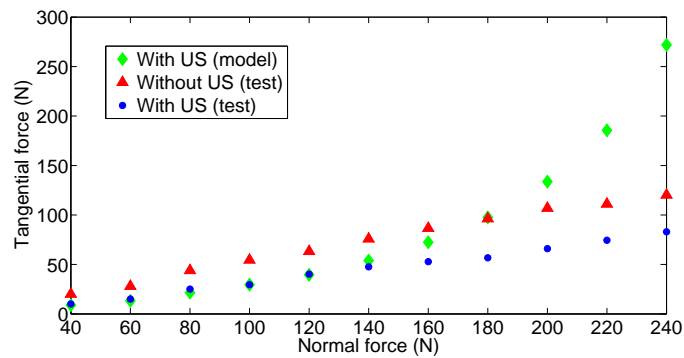


Figure 11. Comparison of friction forces from test results and model simulations.

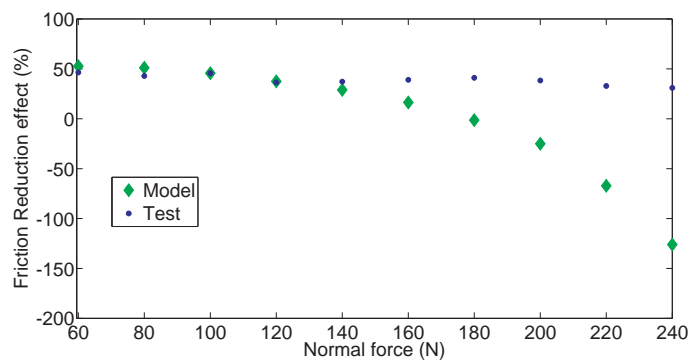


Figure 12. Comparison of friction reduction from test results and model simulations.

combination and normal loading, in the range from 30% to 60%. The net motor forces increase when the normal load increases and the relationship follows a linear trend. The vibratory response of the horn was analyzed and a “cube” contact model was developed. The model simulation shows a close match with the test results under the condition that the normal load is under 120 N.

## REFERENCES

- [1] Mason, W. P., [*Physical acoustics and the properties of solids*], Van Nostrand, 163-168, Princeton, N. J. (1958).
- [2] Pohlman, R. and Lehfeltdt, E., “Influence of ultrasonic vibration on metallic friction,” *Ultrasonics* **4**(4), 178-185 (1966).
- [3] Littmann, W. , Storck, H., and Wallaschek, J., “Sliding friction in the presence of ultrasonic oscillations: superposition of longitudinal oscillations,” *Arch. Appl. Mech.* **71**, 549-554 (2001).
- [4] Littmann, W. , Storck, H. and Wallaschek, J., “Reduction in friction using piezoelectrically excited ultrasonic vibrations,” *Proc. SPIE* **4331**, 302 (2001).
- [5] Bharadwaj, S. and Dapino, M. J., “Effect of load on active friction control using ultrasonic vibrations,” *Proc. SPIE* **7290**, 72900G (2009).
- [6] Bharadwaj, S. and Dapino, M. J., “Friction control in automotive seat belt systems by piezoelectrically generated ultrasonic vibrations,” *Proc. SPIE* **7645**, 76450E (2010).
- [7] Graff, K. F. “Wave motion in elastic solids,” *Clarendon press*, Oxford, (1975).
- [8] Craig, R. C. “Mechanics of Materials,” *John Wiley & Sons*, New York. (2000).
- [9] Bhushan, B. “Introduction to tribology,” *John Wiley & Sons*, New York, (2002).

- [10] Chang, W.R., Etsion, I. and Bogy, D.B., "An elastic-plastic model for the contact of rough surfaces," *ASME J. Tribol*, **109**, 257-263 (1987).
- [11] Chang, W.R., Etsion, I. and Bogy, D.B., "Static friction coefficient model for metallic rough surfaces," *ASME J. Tribol*, **110**, 57-63 (1988).
- [12] Polycarpou, A. A., and Etsion, I., "Analytical Approximations in Modeling Contacting Rough Surfaces," *ASME J. Tribol*, **109**, 257-263 (1999).
- [13] Shi, X., and Polycarpou, A. A., "Measurement and Modeling of Normal Contact Stiffness and Contact Damping at the Meso Scale," *ASME J. Tribol*, **127**, 52-60 (2005).